International Journal of Rock Mechanics & Mining Sciences 176 (2024) 105689

Contents lists available at ScienceDirect

International Journal of Rock Mechanics and Mining Sciences

journal homepage: www.elsevier.com/locate/ijrmms

Numerical modeling of hydraulic stimulation of fractured crystalline rock at the bedretto underground laboratory for geosciences and geoenergies

Iman Vaezi [a,b,c,*], Andrés Alcolea [d], Peter Meier [d], Francesco Parisio [a,b,c], Jesus Carrera [b,c], Víctor Vilarrasa [a]

[a] Global Change Research Group (GCRG), IMEDEA, CSIC-UIB, Esporles, Spain
[b] Institute of Environmental Assessment and Water Research (IDAEA), Spanish National Research Council (CSIC), Barcelona, Spain
[c] Associated Unit: Hydrogeology Group UPC-CSIC, Barcelona, Spain
[d] Geo-Energie Suisse AG, Zürich, Switzerland

ARTICLE INFO

Keywords:
Enhanced geothermal system
Hydroshearing
Fracture variable permeability
Viscoplastic embedded model
Dilatancy
Induced microseismicity

ABSTRACT

Hydraulic stimulation of Enhanced Geothermal Systems (EGS) aims at boosting permeability to facilitate fluid circulation, while keeping a low induced seismicity. However, some stimulations have led to poor permeability enhancement or too high induced earthquakes, which suggests that further understanding is needed on poro-mechanical processes during stimulation. Here, we model a highly-monitored test performed at the Bedretto Underground Laboratory to investigate the impact of fluid injection on permeability enhancement and induced microseismicity. We examine three models: (1) a homogeneous fracture whose transmissivity is manually calibrated to reproduce the observed pressure evolution at the injection borehole (this model fails to capture the spatial distribution of pressure and the corresponding poromechanical processes); (2) an elastic fracture approach, where transmissivity changes locally as a function of fracture aperture following the cubic law (this model overestimates pressure after the onset of fracture slip); and (3) a viscoplastic fracture approach with strain weakening and dilatancy that yields an additional permeability enhancement after shear reactivation. The viscoplastic model captures the spatio-temporal coupled response of the fractured rock to hydraulic stimulation before and after shearing both in terms of pressure and microseismicity. Subsequently to the onset of shear failure, microseismic events occur in every injection cycle as the reactivation front advances when plastic strain and, thus, permeability surpass the previously achieved maximum value. This viscoplastic model permits estimating the extent of the stimulated fracture, the permeability enhancement and its impact on the local state of stress and pore pressure at surrounding fractures, representing a useful tool for the design of effective hydraulic stimulation.

1. Introduction

A global trend towards CO_2 and nuclear-free technologies has promoted interest in deep geothermal energy as an alternative renewable source, free from seasonal fluctuations and, thus, with a potential for continuous energy output.[1,2] Geothermal energy production has been successful in locations with favorable geological conditions such as volcanic fields, hydrothermally active areas, or sedimentary basins with deep-seated permeable rock formations. Enhanced (or Engineered) Geothermal Systems (EGS), previously referred to as Hot Dry Rock or Petrothermal Systems, are envisioned as a way to tap heat from any place in the territory.[3,4]

The goal of EGS is the exploitation of regions with relatively high geothermal gradients through the creation (hydrofracturing) or reactivation (hydroshearing) of a fracture network of sufficient permeability to enable fluid circulation.[5–8] The temperature necessary to produce electricity, i.e., >150 °C, is found at depths greater than 4–6 km, which is typically within the crystalline basement. The crystalline basement is assumed to be critically stressed.[9] Therefore, fluid injection concerns not only rock mass permeability, but also crustal strength and deformability, and ultimately fault instability and induced seismicity.[10–12]

To enhance permeability, injection-induced shear slip and dilation of preexisting fractures have been recognized as the most promising approach for extracting geothermal energy from hot ultralow-

* Corresponding author. Global Change Research Group (GCRG), IMEDEA, CSIC-UIB, Esporles, Spain.
E-mail address: iman.vaezi@csic.es (I. Vaezi).

https://doi.org/10.1016/j.ijrmms.2024.105689
Received 19 June 2023; Received in revised form 21 January 2024; Accepted 24 February 2024

permeability rocks at depth.[13,14] Shear reactivation of fractures/faults caused by pressurized fluid injection is of utmost importance in many subsurface engineering problems and reservoir stimulation,[15–17] particularly with regard to induced microseismicity.[18–24] It is referred to as shear stimulation or hydroshearing in EGS in which, contrary to the hydrofracturing process (which involves short-duration high-pressure injection and proppant usage), the injection pressure aims at causing shear slip and dilation of existing rough fractures.[25,26] This fracture self-propping by asperities is considered an effective means of permanently enhancing permeability.[27–29] Furthermore, new cracks can be created because shear slip increases the stress intensity at the tips of preexisting fractures, potentially leading to fracture propagation and/or generating fracture networks.[19,30–32] The main challenge is to develop adequate permeability in the reservoir while retaining sufficient heat transfer area and keeping the magnitude of induced seismicity as low as possible during reservoir stimulation.[22,33,34] Understanding the governing processes is of utmost importance to improve, and ultimately standardize, the applicability of EGS shear stimulation.[35]

Although the process of shear stimulation is theoretically well understood and routinely modeled, fundamental investigations through laboratory tests and field measurements have been limited. Laboratory-scale experiments can provide an understanding of coupled processes pertinent to the shear stimulation but suffer from test conditions as well as scalability that might lead to oversimplified fracture flow that is not representative of a heterogeneous rock mass. Guglielmi et al. (2015a, 2015b) completed two mesoscale reactivation tests by injecting high-pressure fluid into carbonate and shale faults. One of the insights achieved from these in situ reactivation tests is that aseismic/seismic shear slip by fluid injection enhanced the conductivity of the faults.[20,36] Another intermediate-scale hydro-shearing experiment was executed in the naturally fractured and faulted crystalline rock mass at the Grimsel Test Site (Switzerland) in 2017.[37–39] One of the key findings of this experiment is that initially low-transmissivity structures were stimulated more productively compared with structures of higher initial transmissivity. However, these field tests were conducted on faults and fractured zones at a relatively shallow depth (<600 m), i.e., in rocks with relatively low confinement and low enthalpy potential.

Considering the necessity of an experiment with more similar conditions to intermediate and high enthalpy geothermal systems, the Bedretto Underground Laboratory for Geosciences and Geoenergies (BULGG) hosts medium to large-scale in-situ experiments with a focus on hydraulic stimulation and fault reactivation and associated induced seismicity (Fig. 1). These experiments aim at developing effective and safe hydraulic stimulation protocols to enhance permeability at a controlled risk of induced seismicity for creating an EGS. The overburden directly above the laboratory is approximately 1500 *m*, providing conditions that start to resemble realistic EGS systems (scale 1:3 approximately).[40,41] To characterize the rock mass, several boreholes were drilled perpendicular to the tunnel axis with lengths ranging from 100 m to 400 m MD (Measured Depth). An additional set of short 30-40 m-long vertical boreholes were drilled, for conducting mini-frac tests aimed at quantifying the local state of stress.[42] A suite of hydraulic stimulation tests has been performed at the BULGG to stimulate the fractures intersected by the long boreholes MB1, ST1 and ST2 (Fig. 1). Stress measurements by hydraulic fracturing technique indicate that the BULGG is in a normal faulting - strike-slip stress regime and that the rock mass is close to critically-stressed.[42–46]

This paper aims at numerically modeling and analyzing the hydraulic stimulation performed in borehole MB1 (in blue in Fig. 1c) at the BULGG in February 2020. Numerical simulation is an essential method to investigate coupled hydromechanical processes and to better understand the fundamental mechanisms and feedbacks that occur in geothermal reservoirs. This understanding is particularly important due to the coupling of permeability and fracture aperture.[48] We present three numerical models with increasing complexity (in terms of material constitutive law and coupling of permeability and fracture aperture), which we find to get progressively closer to the conceptual model representing the behavior of the system. Then, we compare numerical results with field experiment data and discuss the implications. Based on the best model, we extend our analysis to poromechanical processes occurring during the stimulation and discuss our findings. Simulation results reveal the extent of the stimulated fracture and permanent permeability enhancement and show that hydroshearing in the stimulated fracture has a non-negligible impact on the stability of adjacent joints due to stress redistribution, which may affect their subsequent stimulation.

2. Methodology

2.1. Numerical models

The numerical model is a 2D hydromechanical plane-strain inclined plane that contains the boreholes that, on average, dip 42° downwards to the southwest (Fig. 1). Thermal effects have been neglected because of the long term ventilation of the gallery, which causes a local “cold” area driven by thermal drainage to the tunnel. Consequently, temperatures are relatively homogeneous in the zone of interest and the temperature of the water injected in the system is that of the gallery (and therefore,

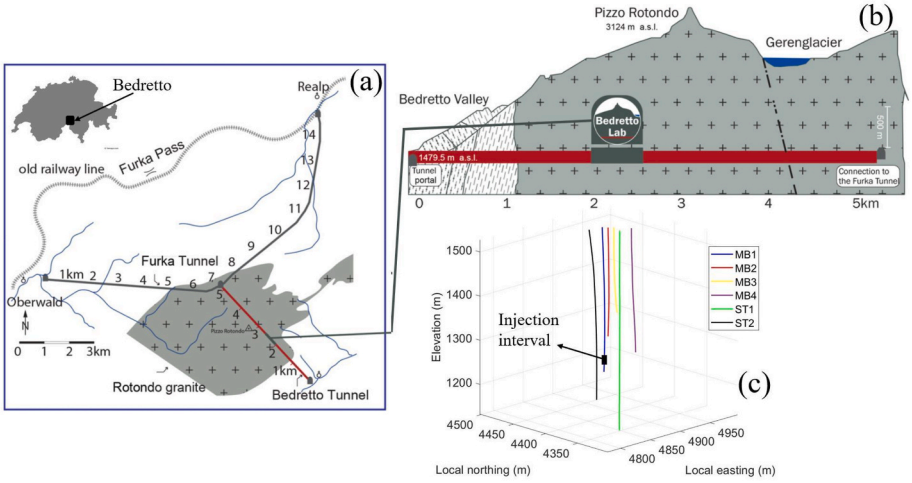

Fig. 1. a) Top view of the Bedretto gallery and the hosting Rotondo granite; b) SE to NW cross-sectional view of the Bedretto lab; c) 3D view of the longest boreholes. Adapted from[45,47].

very similar to the temperature at its surroundings). The model is refined at its center, which represents the BULGG and its vicinity, and grows to a large extension (75 km^2; Fig. 2), beyond the whole Bedretto gallery (top center of the model) to avoid spurious boundary effects. For similar reasons, the bottom boundary is at a true vertical depth of 5000 m (y = −7472.4 m in the inclined plane). Both sides and the bottom of the model are fixed against lateral and vertical displacements, respectively. A linear distributed fluid pressure and initial stresses are applied to the model from top to bottom (Fig. 2a). The major fractures and shear zones identified through borehole logging and geological structural analysis are included in the model.[40,45] The fractures have been modeled as upscaled elastic continuum media with different hydromechanical properties but homogeneous in their space. The mesh also includes the main boreholes (MB1 to MB4, ST1, and ST2 with 20 cm thickness) and is highly refined at the closest vicinity of the modeled fractures and the boreholes. Overall, the mesh consists of 27,248 quadrilateral elements with corresponding 27,420 nodes (Fig. 2d).

Three models were built upon this common set-up. In the first model (termed here model EP, for "Elastic Prescribed transmissivity") the permeability of the main fracture crossing the injection interval (in red in Fig. 2c) has been assigned (homogeneous all along the fracture, but variable in time) to achieve a reasonable fit of the measured pressure evolution at the injection interval. However, changes in fracture aperture occur mainly in the vicinity of the injection interval as a result of injection-induced overpressures. Hence, the second model (model EE, "Elastic Embedded") incorporates the "embedded model", in which permeability is a function of volumetric strain described in section 2.4. In this second model, fracture permeability varies with distance from the injection interval and remains constant and equal to the initial value far away from it, where pressurization has not dilated the fracture. While this approach allows obtaining a good reproduction of the measured injection pressure at early stages, it fails to provide a good fit once the fracture reactivates and inelastic strains occur. Thus, to account for permeability enhancement induced by dilatancy due to the shear slip of the fracture, the third model (model VE) incorporates a viscoplastic constitutive law that includes dilatancy and strength softening. Table 1 summarizes the main input values for these models and the host rock. Notably, each fracture has different hydraulic and mechanical properties inferred from well logging and hydraulic tests. However, variable permeability is considered only in the stimulated fracture because the main impact at the surrounding fractures is mainly poroelastic but not

Table 1
Hydromechanical properties of the rock matrix (granite) and the stimulated fracture for different tested models.

	Granite	Stimulated fracture		
		EP	EE	VE
Mechanical constitutive behavior	Elastic	Elastic		Viscoplastic
Permeability (k)	2.5×10^{-18} m^2	Prescribed	Embedded model	
Young's modulus (E)	46 GPa	23 GPa		
Poisson ratio (ν)	0.37	0.37		
Porosity (ϕ)	0.005	0.005		
Viscosity (μ)	–	–	–	2.5 GPa s
Peak friction angle (φ_{peak})	–	–	–	23°
Residual friction angle (φ_{res})				20°
Cohesion (c)	–	–	–	0.01 MPa
Dilatancy angle (ψ)	–	–	–	20°
Critical value of the softening parameter (η^*)	–	–	–	0.001

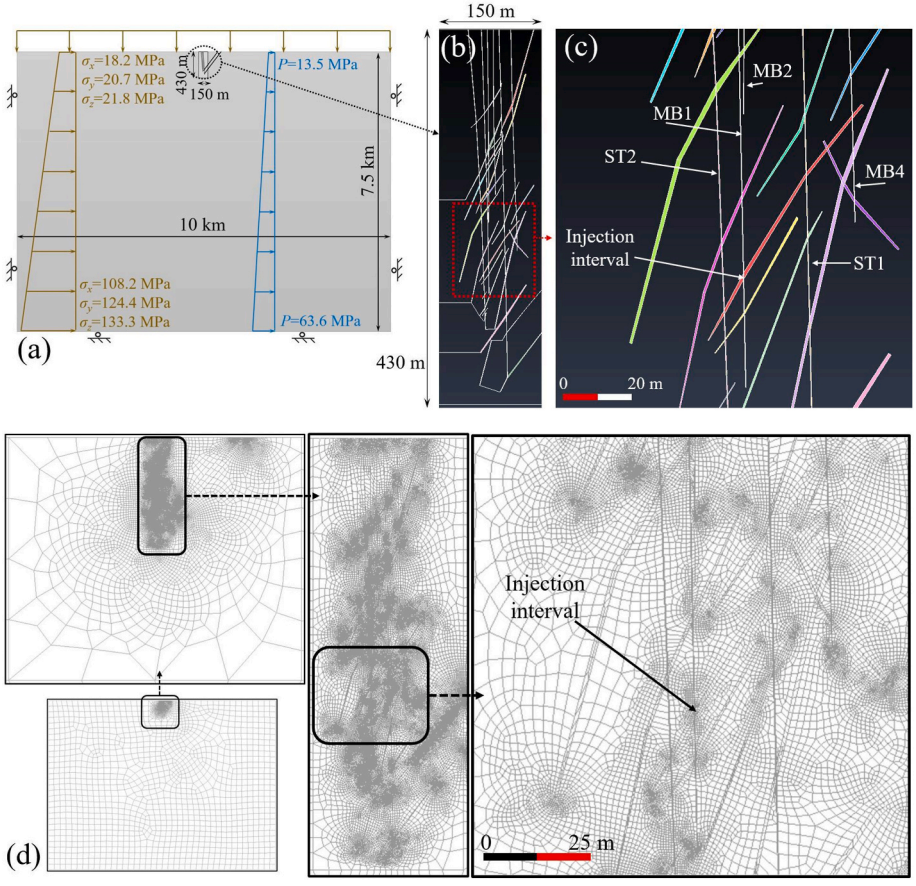

Fig. 2. a) Model geometry and boundary conditions; b) Configuration of boreholes, identified fractures and fault zones; c) Detailed view around the stimulated fracture (in red); d) Mesh configuration from global to detailed view around the stimulated fracture zone.

hydraulic. The hydraulic and mechanical parameters of the surrounding fractures are not relevant to changes in the stimulated fracture induced by injection, which are mainly local and driven by the parameters of the stimulated fracture and surrounding matrix. The fully coupled hydro-mechanical numerical models are implemented using the software CODE_BRIGHT.[49,50]

The models are initialized by simulating the drainage effect of the tunnel on porewater pressure by imposing atmospheric pressure at the top boundary, and the subsequent consolidation, which tends to close fractures. The drainage period spans from the end of the excavation in 1976 until now. As such, the initial decompression of the system caused by excavation is not considered because its transient effects are small, as shown in a prior sensitivity analysis. In the same line of arguments, the drilling of boreholes is not modeled explicitly. Subsequently, the stimulation test (in February 2020, being the first one in a series of many at the BULGG) is modeled by injecting water through an isolated section of borehole MB1, at a measured depth of 267 m (true vertical depth 188.8 m), into the fracture (in red in Fig. 2c). Isolation was achieved by a double packer, also included in the model as a very stiff and low-permeability section of the borehole ($E = 4600$ MPa, $k = 2.5 \times 10^{-18}$ m^2, after inflation). The permeability of the boreholes, also modeled explicitly, is $k = 2.5 \times 10^{-14}$ m^2. The numerical simulations cover the first 3.4 h of the field experiment, during which we compare the outcomes of the three models with the experimental results. Results of model VE are extended in time up to the first 8 h of the experiment.

2.2. Governing equations

The mechanical problem is solved by satisfying the momentum balance. Neglecting inertial terms, the momentum balance reduces to the equilibrium of stresses,

$$\nabla\cdot\boldsymbol{\sigma} + \mathbf{b} = \mathbf{0} \tag{1}$$

where $\boldsymbol{\sigma}$ [ML^{-1}T^{-2}] is the total stress tensor and $\mathbf{b}$ [ML^{-2}T^{-2}] is the vector of body forces.

In linear elasticity theory for continuous media, the relationship between stress, strain, and fluid pressure for isotropic materials is given by Hooke's law,

$$\Delta\boldsymbol{\sigma} = K\varepsilon_v\mathbf{I} + 2G\left(\boldsymbol{\varepsilon} - \frac{\varepsilon_v}{3}\mathbf{I} + \frac{\alpha}{2G}\Delta p_f\mathbf{I}\right), \tag{2}$$

where ε_v [−] is volumetric strain, $\mathbf{I}$ [−] is the identity matrix, $\boldsymbol{\varepsilon}$ [−] is the strain tensor, $K = \frac{E}{(3(1-2\nu))}$ [ML^{-1}T^{-2}] is the bulk modulus, $G = \frac{E}{(2(1+\nu))}$ [ML^{-1}T^{-2}] is the shear modulus, E [ML^{-1}T^{-2}] is Young's modulus, ν [−] is the Poisson ratio, p_f [ML^{-1}T^{-2}] is fluid pressure, and α [−] is the Biot effective stress coefficient. In this work, we assume $\alpha = 1$,[43] which leads to the strongest hydromechanical coupling.[51]

Equation (2) is coupled with the flow equation through fluid pressure. Assuming that there is no external loading and neglecting the compressibility of the solid phase, fluid mass conservation can be written as

$$\frac{\Phi}{K_f}\frac{\partial p_f}{\partial t} + \frac{d}{dt}(\nabla\cdot\mathbf{u}) + \nabla\cdot\mathbf{q} = 0, \tag{3}$$

where Φ [−] is porosity, K_f [ML^{-1}T^{-2}] is water bulk modulus, t [T] is time, $\mathbf{u}$ [L] is the displacement vector, $\mathbf{q}$ [L^{3}T^{-1}] is the water flux, given by Darcy's law, and d/dt denotes material derivative. Note that the flow (Eq. (3)) and mechanical (Eq. (2)) equations can be also coupled through the volumetric strain (second term in the left-hand side of Eq. (3)), which can be expressed as the divergence of the displacement vector.

2.3. Fracture constitutive model

Fracture reactivation is modeled by a viscoplastic constitutive law in which fracture failure is given by the Mohr-Coulomb criterion and includes dilatancy and strain softening.[52,53] The yield function (F) and the flow rule (G) are defined as

$$F = p\cdot\sin\varphi(\eta) + \left[\cos\theta - \frac{1}{\sqrt{3}}\sin\theta.\sin\varphi(\eta)\right]\cdot\sqrt{J_2} - c(\eta)\cdot\cos\varphi(\eta), \tag{4}$$

$$G = \xi\cdot p\cdot\sin\psi + \left(\cos\theta - \frac{1}{\sqrt{3}}\sin\theta\cdot\sin\psi\right)\cdot\sqrt{J_2} - c(\eta)\cdot\cos\varphi(\eta), \tag{5}$$

where p [ML^{-1}T^{-2}] is the mean stress, J_2 [ML^{-1}T^{-2}] is the second invariant of the deviatoric stress tensor, η [−] is the softening parameter, ξ [−] is a parameter for the plastic potential, φ [°] is the friction angle, c [ML^{-1}T^{-2}] is cohesion, and ψ [°] is the dilatancy angle. The invariant θ [°] is defined as

$$\theta = \frac{1}{3}\sin^{-1}\left(-\frac{3\sqrt{3}}{2}\frac{J_3}{J_2^{3/2}}\right), -30^\circ \le \theta \le 30^\circ, \tag{6}$$

where J_3 [ML^{-1}T^{-2}] is the third invariant of the deviatoric stress tensor. The stress function $T(F)$ is[52]

$$T(F) = F^m \; for \; F \ge 0, T(F) = 0 \; for \; F < 0, \tag{7}$$

where m [−] is a constant power, chosen equal to 3 here.[54,55] Both the cohesion and the friction angle can depend on the softening parameter (η) as

$$\lambda(\eta) = \begin{cases} \lambda^{peak} & \eta \le 0 \\ \lambda^{peak} + \left(\dfrac{\lambda^{res} - \lambda^{peak}}{\eta^*}\right)\cdot\eta & 0 \le \eta \le \eta^* \\ \lambda^{res} & \eta^* \le \eta \end{cases}, \tag{8}$$

where λ represents either cohesion (c) or friction angle (φ), and λ^{peak} and λ^{res} are user defined peak and residual values, respectively (see Table 1). As shown in Table 1, cohesion is low and we assume a constant value equal to 0.01 MPa. η^* is the value of the softening parameter controlling the transition between the softening and residual stages. The softening parameter depends on plastic strain as

$$\eta = \sqrt{\frac{3}{2}\left[\left(\varepsilon_x^p - \varepsilon_m^p\right)^2 + \left(\varepsilon_y^p - \varepsilon_m^p\right)^2 + \left(\varepsilon_z^p - \varepsilon_m^p\right)^2 + \left(\frac{1}{2}\gamma_{xy}^p\right)^2 + \left(\frac{1}{2}\gamma_{yz}^p\right)^2 + \left(\frac{1}{2}\gamma_{zx}^p\right)^2\right]}, \tag{9}$$

where $\varepsilon_m^p = \frac{1}{3}(\varepsilon_x^p + \varepsilon_y^p + \varepsilon_z^p)$ [−] is the mean plastic strain, and ε and γ are the diagonal and off-diagonal terms of the plastic strain tensor.

The quantification of shear slip tendency and proximity to shear failure conditions can be calculated with the mobilized friction angle. Shear failure occurs when the mobilized friction angle equals the actual friction angle. An alternative means of representing mobilized friction resistance, without implying a specific spatial orientation, involves expressing it in terms of invariants of the effective stress tensor. Considering the mean effective stress p' and deviatoric stress q, the mobilized friction angle can be expressed as

$$\varphi_{mob} = \sin^{-1}\left(\frac{3M}{6+M}\right), \tag{10}$$

where $M = \frac{q}{p}$ is the slope of the stress path curve in the p'-q diagram.

2.4. The embedded model

The modeled fracture was identified in the lithological and image logs and in cores retrieved during the drilling of borehole MB1. This zone is a composite of several smaller fractures embedded in a matrix material. The permeability of the stimulated fractured zone is computed

using the cubic law,[56] which makes fracture transmissivity proportional to b^3 (b being the aperture). Since CODE_BRIGHT adopts a small displacements approach, the geometrical grid aperture is fixed. Therefore, actual aperture changes, which are proportional to volumetric strain, are modeled by changing permeability as

$$k = k_m + \frac{(b_0 + a\Delta\varepsilon)^3}{12a}, \tag{11}$$

where k_m [L^2] is the intrinsic permeability of the matrix within the fracture zone (in red in Fig. 2c), a [L] is the spacing between the fractures within the fracture zone, b_0 [L] is the initial fracture aperture, $\Delta\varepsilon$ [−] is the volumetric strain change ($\Delta\varepsilon = \varepsilon - \varepsilon_0$), and ε_0 [−] is a threshold value. For the stimulated fracture zone, the following parameters are considered: $k_m = 5{\cdot}10^{-17}$ m^2, i.e., 20 times larger than that of surrounding granite, $b_0 = 2.25{\cdot}10^{-6}$ m, $a = 0.01$ m, and $b_{max} = 1.34{\cdot}10^{-4}$ m, which is the maximum aperture (upper bound of aperture), above which fracture permeability stops increasing.

3. Results

3.1. Reproduction of measured injection pressures

In the EP model, the temporal evolution of the permeability of the stimulated fracture is manually adjusted as constant during each injection interval so as to reproduce the observed injection pressure each interval. Although the overall model fit is good up to 2.5 h of injection (green dotted line in Fig. 3a), it fails to reproduce the shape of the pressure curve in each injection step, in which pressure sharply increases at the beginning and the subsequent pressure build-up diminishes smoothly with time under constant flow rate (note that the first steps, until t~1.3 h were intended to be constant pressure head tests). In short, the EP model fits well the beginning and end pressures for each step, but not the intermediate evolution. As discussed below, this discrepancy reflects that permeability changes are imposed for the whole fracture and not just for the actually stimulated region, which results in an unrealistic rapid pressure propagation along the whole fracture (Fig. 4a).

The EE model (Eq. (10)) accounts for both the spatial and temporal evolutions of fracture transmissivity in response to deformation. The brown curve in Fig. 3a depicts the temporal evolution of generated overpressure at the injection interval predicted by the model with variable permeability as a function of fracture aperture (EE model). This

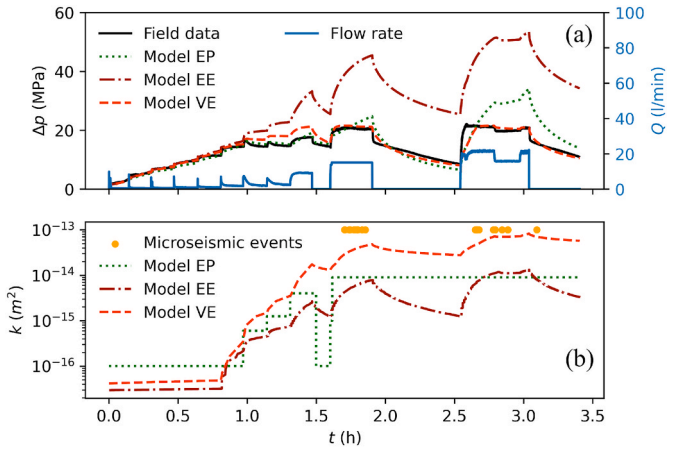

Fig. 3. a) Temporal evolution of calculated and measured overpressure (i.e., above formation pressure) at the injection borehole; b) Temporal evolution of fracture permeability in models with prescribed and variable permeability near the injection interval (point 1 in Fig. 6c) and timestamps of observed induced microseismicity events.

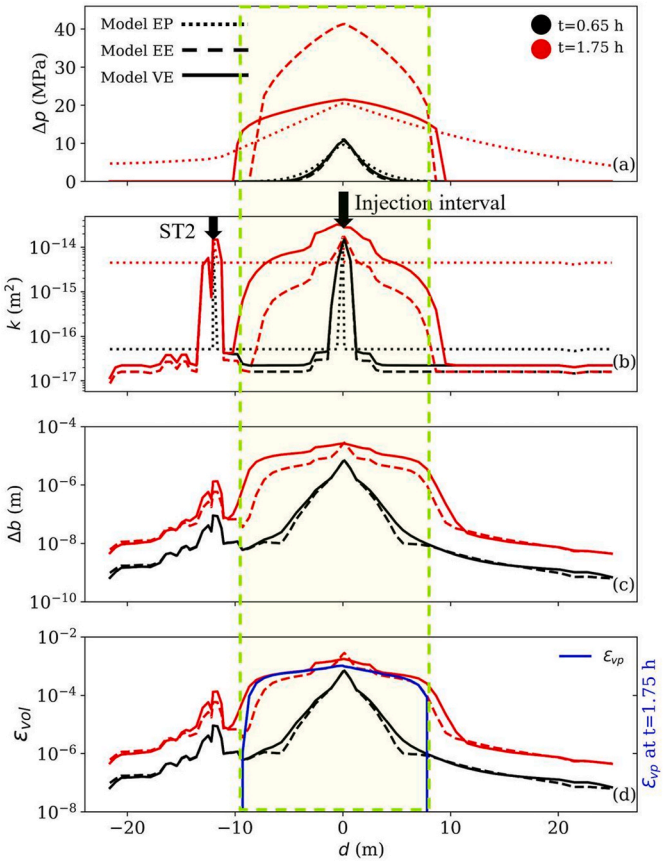

Fig. 4. Profiles along the stimulated fracture of a) pressure build-up, b) fracture permeability, c) fracture aperture change ($b_0 = 2.25{\cdot}10^{-6}$ m), and d) volumetric strain (and volumetric plastic strain (ε_{vp}) at t = 1.75 h for model VE). Results are displayed at two moments for all models. The injection interval is located at d = 0 and is positive upwards. Note the intersection with well ST2 around d = −12 m (Fig. 2c).

model can accurately reproduce the field test results until 0.7 h. We attribute subsequent discrepancies to fracture dilatancy caused by slip, which leads to an additional, and irreversible, permeability enhancement. The elastic nature of this model cannot reflect this irreversible hydromechanical response. Consequently, the generated strain is smaller than the actual one, and the embedded model EE yields less permeability enhancement than the actual one. As a result, the calculated overpressure is higher than the measured one at late times, when slip has become significant. This limitation is overcome by the VE model.

Fig. 3b displays the temporal evolution of permeability prescribed (model EP) or calculated (models EE and VE). As observed in Fig. 3a, all models render more or less a good fit with the generated overpressure until around 0.7 h, when the jacking pressure is achieved and the initially tight fracture gets opened, which leads to (1) the first sudden pressure drop (Fig. 3a), and (2) the corresponding sudden permeability increase (Fig. 3b). The sudden increases in storage capacity and permeability hindered the control of pressure, which tended to drop. Therefore, the injection protocol was changed to constant flow rate injection at 1.3 h. A first shut-in at $t = 1.5$ h led to a sudden drop of fracture permeability. Notably, the permeability drop required by the EP model to still reproduce the measured injection pressure is way larger than those calculated by the EE and VE models, what confirms the need to accommodate spatial variability in permeability enhancement. During the two additional shut-in episodes until $t = 3.4$ h, the EE model shows a severe permeability reduction compared to the VE model, which reveals the need to accommodate permanent enhancement of fracture

permeability.

The VE model reproduces the temporal evolution of injection overpressure better than previous models, especially during the last injection phase ($t > 2.5$ h). The VE model allows to simulate fracture reactivation and yields an additional and permanent permeability enhancement when compared with the elastic models EP and EE. In this case, permeability enhancement is given by both elastic and plastic strains as slip accumulates. Plastic strain further enhances fracture permeability, leading to smaller pressure build-ups and thus, to a better approximation of field data. Permeability enhancement is one order of magnitude larger for the viscoplastic model than for the elastic model. Obviously, permeability decreases during shut-in periods (associated to closure of the elastic portion of strain), but a significant fraction of the permeability enhancement is permanent, thus contributing to improved borehole injectivity. This behavior has been observed, e.g., in Basel, by comparing data acquired during the stimulation carried out in 2006 with that of hydrotests carried out years later, in 2009[57,58] (Alcolea and Meier, personal communication). Note that the timestamps of located microseismic events (Fig. 3b) correspond approximately to the times of maximum permeability enhancement. This observation will be further discussed later.

The main limitation of the EP model, beyond the arbitrariness in manually modifying permeability, is that fracture permeability is homogeneous at any given time (Fig. 4b). Using an embedded model (in which permeability is a function of volumetric strain) shows that permeability increases locally near the injection borehole and that the enhancement is lower away from the well. The longitudinal profile of fracture permeability displays an increase (around 3 orders of magnitude at maximum, Fig. 4b) in fracture permeability due to the increase in fracture aperture (Fig. 4c). Note that permeability enhancement occurs within the pressurized region of the fracture (Fig. 4a). However, the permeability enhancement is moderate, with permeability remaining below 10^{-14} m^2 in EP and EE models, and thus, the predicted pressure build-up becomes excessively high compared to field measurements at late times (Fig. 3). Considering shear failure and dilatancy yields an additional increase in fracture permeability of one order of magnitude that permits reproducing the measured pore pressure evolution at the injection borehole.

The pore pressure build-up along the stimulated fracture (Fig. 4a) mainly occurs within the reactivated region with irreversible strain (highlighted in green; Fig. 4d). Fig. 4a displays the fact that even though the EP model can reproduce measured pressures as good as the VE model at the injection borehole, pressure profiles along the fracture are significantly different. The EP model underestimates the pressure buildup within the reactivated region and overestimates it away from the reactivated region. Until 1.75 h of injection, fracture aperture has already dilated and opened around 10 μm in the reactivated fracture patch (VE model, solid red line in Fig. 4c). Model VE gives insights of the actual pore pressure distribution within the fracture.

3.2. Fracture reactivation

The contour plots of pore pressure at several stages of the stimulation (Fig. 5) reveal that adjacent fractures and wellbores start to be pressurized after 2.6 h of stimulation. The pressurization becomes significant outside the stimulated fracture during the last phase of stimulation ($t =$

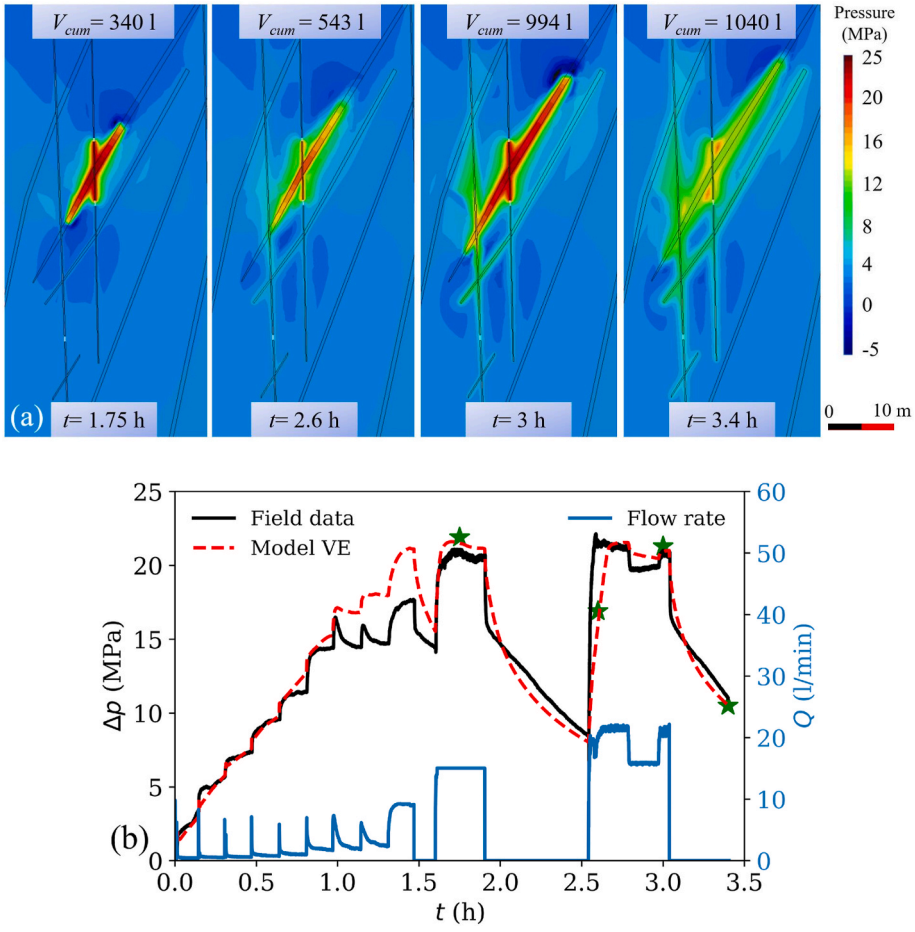

Fig. 5. a) Contour plots of pore pressure at four stages of the stimulation (indicated with green stars in b) with the corresponding cumulative injected fluid volume V_{cum} using the VE model. b) Observed and simulated pressure evolution and injection flow rate at the injection borehole.

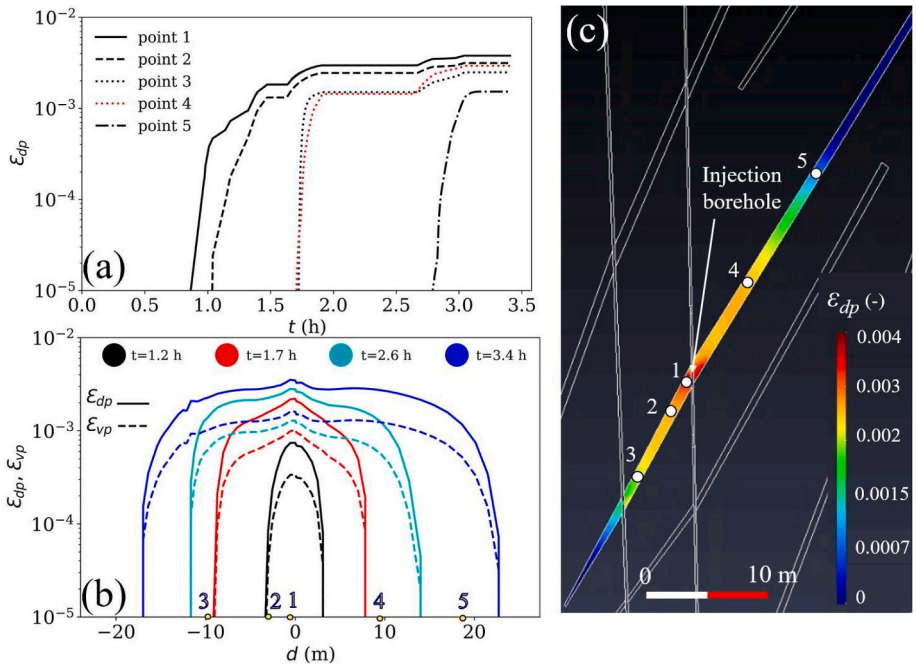

Fig. 6. a) Temporal evolution of the deviatoric plastic strain at five points in the fracture (indicated in panel c); b) Profiles of deviatoric and volumetric plastic strains (ε_{dp} and ε_{vp} respectively) along the fracture at four times of the simulation (color coded with respect to time), the location of the monitoring points are indicated on the x axis; c) Contour plot of deviatoric plastic strain in the stimulated fracture at t = 3.4 h. The five observation points are indicated on the x axis in panel b.

3 h in Fig. 5), when shearing has become relevant. This overpressure includes the low-permeability rock matrix and becomes marked after shearing, which indicates that it is largely driven by poroelastic effects (analytical solutions are available to gain insight into these effects[59]). These effects overlap with hydraulic connectivity (pressure diffusion) along fractures, apparent from the reduced pressure gradient along fractures in Fig. 5. Hydraulic connection causes a non-negligible leak--off, which may be responsible for water back-flow into the injection wellbore outside the isolated interval. Bypass (back-flow to the section above the upper packer) was measured in the field during most stimulation experiments in BULGG. Leak-off can also be detected in the diagnostic plots of such stimulations (Alcolea and Meier, personal communication) by observing the derivative of injection pressure with respect to log-time as a function of time, which correlates well with the flow dimension n.[60,61] The flow dimensions are, in most cases, initially linear to bilinear (n = 1 to 1.5), followed by an infinite acting radial flow period (n~2) during which flow occurs mainly along the fracture, and finally by a spherical flow period (n=2 to 3), which reveals the pressurization of the surrounding area and flow the overall medium via nearby fractures and boreholes.

Realism of the VE model is further supported by the antisymmetric changes in pressure at the edges of the shearing region. Extension occurs away from the shearing tip at the side displacing towards the injection point (left side of the fracture at the top and right at the bottom in Fig. 5a). Vilarrasa et al. (2021, 2022)[17,62] argue that this effect is one of the causes of delayed seismicity (aftershocks occurring some time after the main event). These extension zones would tend to fail, but become temporarily stabilized by the pressure drop. This mechanism may contribute to enhanced stimulation beyond the initial fracture and to broad block connectivity. Pressure increases on the other side of the fracture near the tip, thus yielding an antisymmetric poroelastic effect (See Figs. 12 and 13 in the supplementary materials for the contour plots of the effective mean stress and deviatoric stress in the same panel view as the pressure field in Fig. 5a).

Further insight into the microseismicity mechanisms can be gained from the evolution of the deviatoric plastic strain during injection (shown for five fracture points in Fig. 6c). The strain sharply rises after failure, coinciding with jacking of the fracture at that location, in all points (Fig. 6a). Once jacking occurs, irreversible strain accumulates at a very low rate. The reactivation front, which coincides with the sharp increase in plastic strain, progressively advances away from the injection borehole. Plastic strain propagates by the end of the simulation (t = 3.4 h) along 45 m of the fracture, i.e., some 20 m away to each side of the injection borehole. Fracture reactivation propagates further upwards than downwards (Fig. 6b). Even though it is common that seismic clouds develop predominantly upwards,[63] in this case, downwards propagation is limited by the presence of borehole ST2, which causes a local reduction in pore pressure because of its high permeability and inhibits further reactivation.

The stress paths of points 1–3 (location shown in Fig. 6c) in the q-p' plane, i.e., deviatoric versus mean effective stress, display trajectories that move towards the failure surface until failure conditions are reached and then, the stress paths move along the failure surface (Fig. 7). Note that the initial stress state is stable in all cases because the drainage of the tunnel increases the effective mean stress. Close to the injection borehole (point 1), the effective mean stress is reduced as liquid pressure increases with a progressive deviatoric stress increase. Further away (points 2 and 3), the deviatoric stress increases more pronouncedly at the beginning of injection because of stress transfer caused by slip of the portion of the fracture located closer to the injection borehole and because the further away a point is located from the injection borehole, the longer it takes to the pressure front to reach that point. Failure occurs under compression in all cases (p'>0). A detailed look on the stress path at point 1 reveals a relation between timestamps of the stress path direction and those of measured induced microseismic events (Fig. 3b). After the activation, the first time when the stress path goes downward left, $t_{1\text{-}1}$=1.64 h, corresponds approximately to the timestamp of the first recorded microseismic event (t=1.704 h). Note that not all recorded microseismic events are plotted in Fig. 3, but only the ones that could be located, i.e., some smaller magnitude events, below the magnitude of completeness of the seismic monitoring work, may have occurred before. Going downward-left lasts until $t_{1\text{-}2}$=1.89 h, which approximately corresponds to the arrest of microseismicity (t=1.875 h). The second one starts at $t_{2\text{-}1}$=2.63 h and lasts until t_{2}.

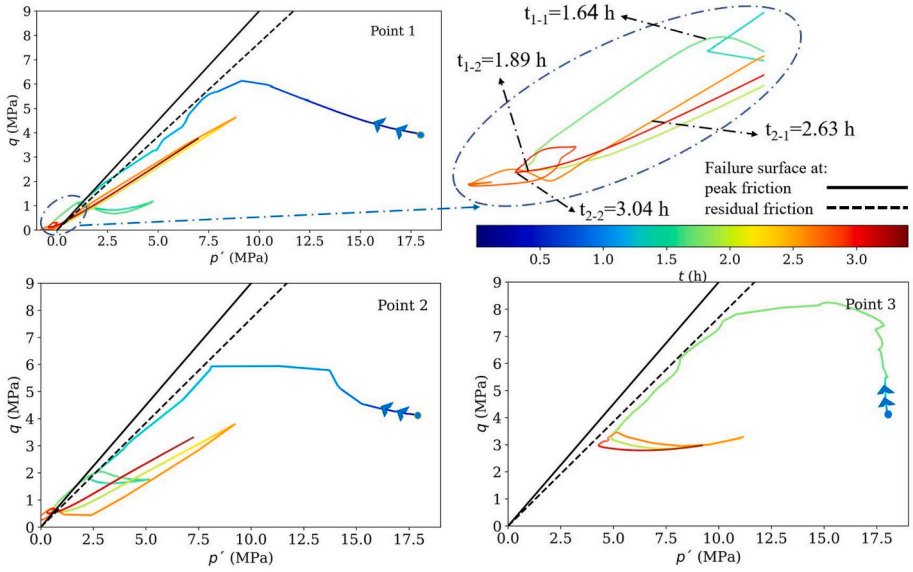

Fig. 7. Effective stress path in the *q*-*p*' plane for the viscoplastic model (VE) and Mohr-Coulomb failure surfaces for points 1 to 3 located along the fracture (see Fig. 6 for their location). The initial yield point indicates the onset of plastic deformation. A zoomed view for stress trajectories at point 1 is provided with time stamps for the change of the stress path. Note that the depicted timestamps correspond to those of begin and arrest of induced microseismicity, as monitored in the field (see Fig. 3b).

$_2$=3.04 h. The second onset of microseismicity (t=2.625 h) happens when the stress path is near the Mohr-Coulomb failure line. The last located event (t=3.093 h) occurs slightly after $t_{2\text{-}2}$, during the shut-in phase. Similar qualitative conclusions are attained by observing the stress path of point 2, located 4.2 m away from the injection interval. In a nutshell, microseismicity develops since the stress path approaches the failure surface until it starts to go away from it. In the field, located seismic events aligned well with the simulated fracture fingerprint and developed (subject to the accuracy of the monitoring network) some 10 m downwards and 40 m upwards. The detailed spatio-temporal correlation between stress paths and timestamps of the located microseismic events is out of the scope of this work.

3.3. Response at nearby fractures

Pressurization of the stimulated fracture causes a poromechanical response of the rock matrix (Fig. 8a) inducing changes in shear stresses that affect nearby fractures (Fig. 8c). Initially, under low injection pressures, the induced shear stresses are reversible and would even vanish shortly after an eventual shut-in. However, once the stimulated fracture is reactivated, an irreversible shear stress drop[64–66] occurs within the slipped fracture patch and the bulbs of positive shear stress are displaced towards its tips. As slip accumulates, the region with shear stress changes extends (see points I and J, at 20 m and 1 m from the stimulated fracture), affecting nearby fractures. Thus, the stimulation of a single fracture may modify also the stability of nearby fractures.[67]

Fig. 8c displays the stress path at eight points located in four nearby fractures. For comparison purposes, all the axes have the same range of values. The failure surface is not plotted because it is placed far away to the left of the displayed paths, i.e., all points are stable during the whole stimulation. Some areas are barely affected by stimulation (points A and B, located far away from the stimulated fracture). In contrast, others experience significant stress changes (up to 3 MPa both in deviatoric and effective mean stress), e.g., points D to F, in the fractures right above and below the stimulated one. Some points approach shear failure conditions, either because of an increase in the deviatoric stress (point A), a decrease in the effective mean stress (point G), or a combination of both (point D). The trajectories are diverse, which highlights the complexity of pore pressure variations and stress changes that occur not only within the stimulated fracture, but also in its surroundings.

Shear failure conditions are also approached by a decrease in the effective mean stress and a slight decrease in the deviatoric stress (point E after 1.5 h of stimulation), which is usually the case when elastic poromechanical stress changes occur as a result of pore pressure increase.[24] Yet, the trajectory at point E is more complex, showing an initial increase in deviatoric stress at constant effective mean stress, followed by a decrease in the deviatoric stress and effective mean stress, which could have been caused by shear-slip stress transfer and subsequent slip-driven pore pressure changes.[17] Other sharp changes in the deviatoric stress are also induced by reactivation of the stimulated fracture (see points D and F). Other areas, affected by the stress shadow, move away from the failure surface by either increasing mean effective stress under constant deviatoric stress (point H) or by decreasing deviatoric stress under constant mean effective stress (point C).

3.4. Including more injection cycles in the viscoplastic model

The parameters of the model VE (Table 1) have been manually adjusted to render a good reproduction of the early stages of the stimulation (up to t=3.4 h, Fig. 3a). We validate the model by adding more injection cycles. The numerical model reproduces pore pressure evolution at the injection borehole fairly well during the validation period (from t=3.4 h to t=8 h; Fig. 9). Thus, we conclude that the VE model reproduces the progressive hydraulic stimulation of the fracture, which enhances permeability away from the injection well as the number of injection cycles accumulates (Fig. 10).

Field measurements display a sharper pressure response at the borehole, both at the onset of injection and after shut-in, which may indicate that jacking of the fracture only occurs after exceeding a certain pressure threshold, which is not fully captured by the numerical model (Fig. 9). It must be acknowledged, however, that compliance effects (response of packers and monitoring devices to the high and fast changes in pressure) also affect data, so we are not overly concerned by sharp responses. The relevant issue is that a number of microseismic events could be located during the field experiment. They coincide with the injection periods as the fracture undergoes slip. However, some occur after shut-in (Fig. 9), as is often the case in practice.[68,69] Microseismic events occur in every injection cycle, when permeability surpasses the

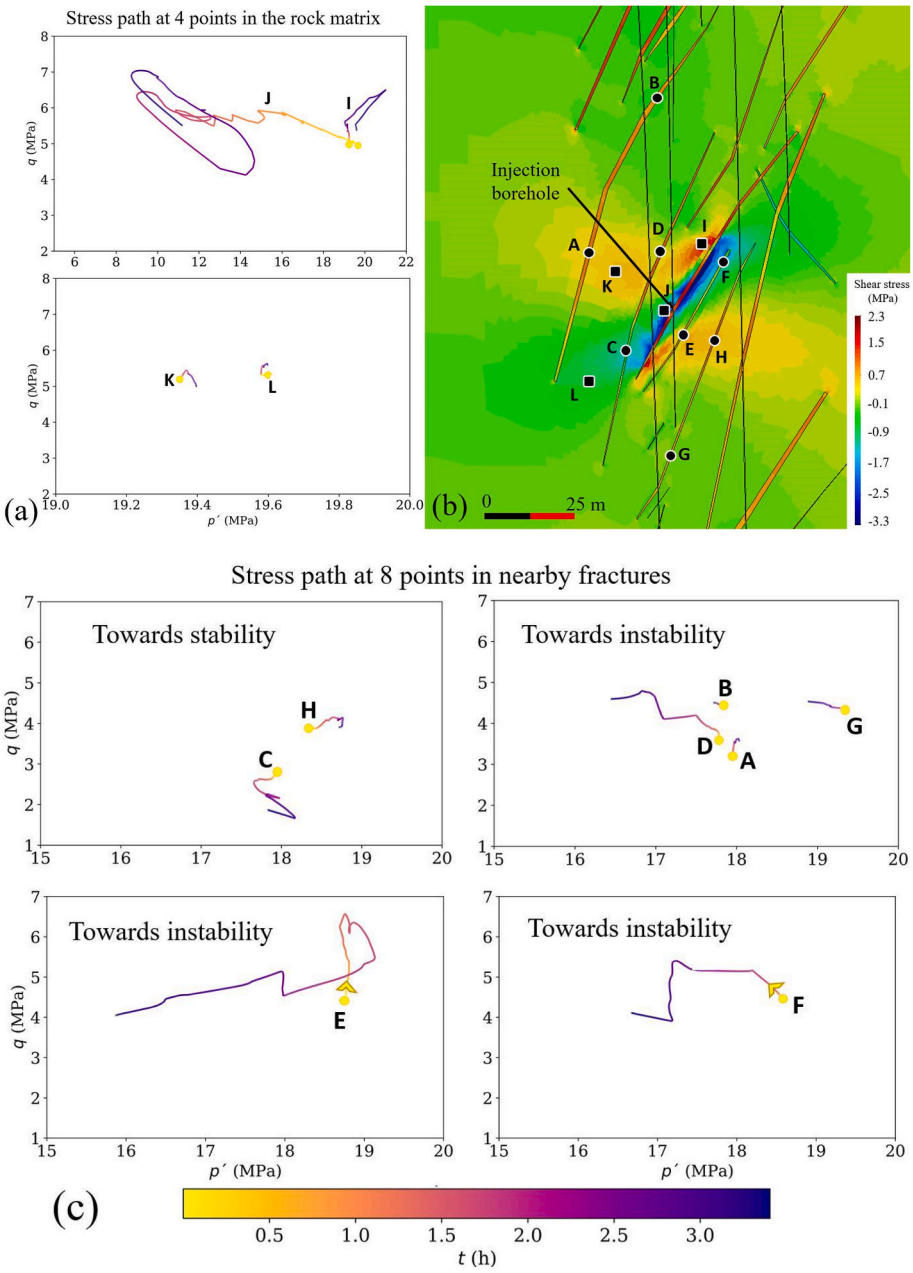

Fig. 8. Stress paths (a) at four points in the rock matrix (I to L, depicted in panel b by squares), and (c) at eight points in nearby fractures (A to H, circles), respectively; the failure surface is located far away on the left side (all points are stable); b) Location of the selected points, with the shear stress (τ_{xy}) after 3.4 h in the background.

previously achieved maximum value (see the permeability evolutions for 8 points located within the stimulated fracture in Fig. 10a), a few examples are indicated with dotted arrows in Fig. 10a and a zoom is provided in Fig. 10b, meaning that the previously reactivated fault patch is reached and the new reactivation is accompanied by microseismic events. This observation is related to the Kaiser effect; materials retain a "memory" of previously applied stresses.[70] In the course of successive hydraulic stimulations, induced seismicity is found to be triggered solely upon surpassing the previous maximum of Coulomb stress changes[71] corroborating our findings. The nucleation process is delayed if the stress decreases and it resumes only upon the return of stress to its previous peak level. In our simulation, permeability enhancement is observed 50 m away from the injection well after t~8 h of injection, coinciding with a final swarm of microseismic events (Fig. 10a). The timestamps of microseismic events correspond well with the times of maximum mobilized friction angle (Fig. 10c). The continuation of the stress path at point 1 (Fig. 7) including more injection cycles in Fig. 11 displays a repetitive recurrence where the periodicity of the fracture reactivation shows the microseismic threshold is concomitant to plasticity.

4. Discussion

The comparison between pore pressure evolution calculated by three models highlights that a viscoplastic model with strength weakening and dilatancy and computing fracture permeability changes as a function of volumetric strain assuming the cubic law (model VE) is needed, to reproduce field observations of hydraulic stimulation of crystalline rock. The elastic (EP and EE) models forecast significantly larger overpressures compared to the measured ones at the timestamps of

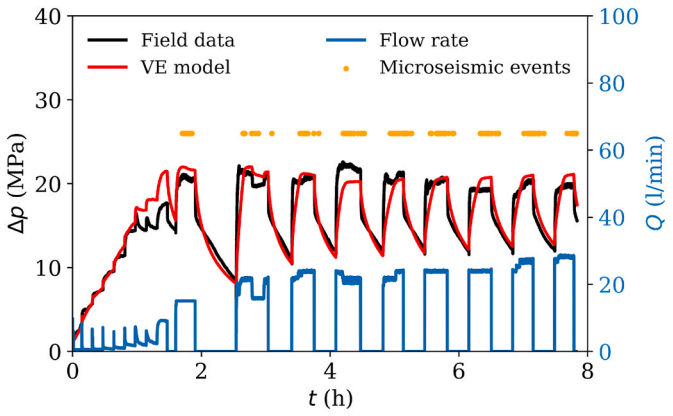

Fig. 9. Temporal evolution of pressure and flow rate at the injection borehole for a large number of injection cycles for model VE compared to the field measurements. The timestamps of located microseismic events are indicated with orange dots.

microseismic events (orange dots in Fig. 3). Thus, according to elastic models, microseismic events after shear failure should have occurred way before. This discrepancy suggests that the fracture was undergoing progressive slip and opening due to dilatancy, and thus permeability enhancement when the microseismic events were monitored. Furthermore, the validity of the implemented conceptual model including viscoplasticity is also confirmed by model validation, i.e., simulating further injection cycles not used for calibrating the model (Fig. 9).

The comparison between permeability profiles along the fracture indicates a greater enhancement of permeability (Fig. 4b) due to the larger dilatancy-induced increase of fracture opening in the viscoplastic model. The permeability enhancement of up to three orders of magnitude extends up to 40 m along the fracture towards the end of the calibration period (t~3.4 h). Fig. 4a highlights the differences in pore pressure along the fracture for the three models once the fracture is reactivated ($t > 0.65$ h). Simulation results show that when the permeability is manually and homogeneously adjusted in the whole fracture (model EP), pore pressure diffuses along the whole fracture, yielding a pore pressure distribution that significantly differs from the actual one. When simulating variable permeability as a function of the

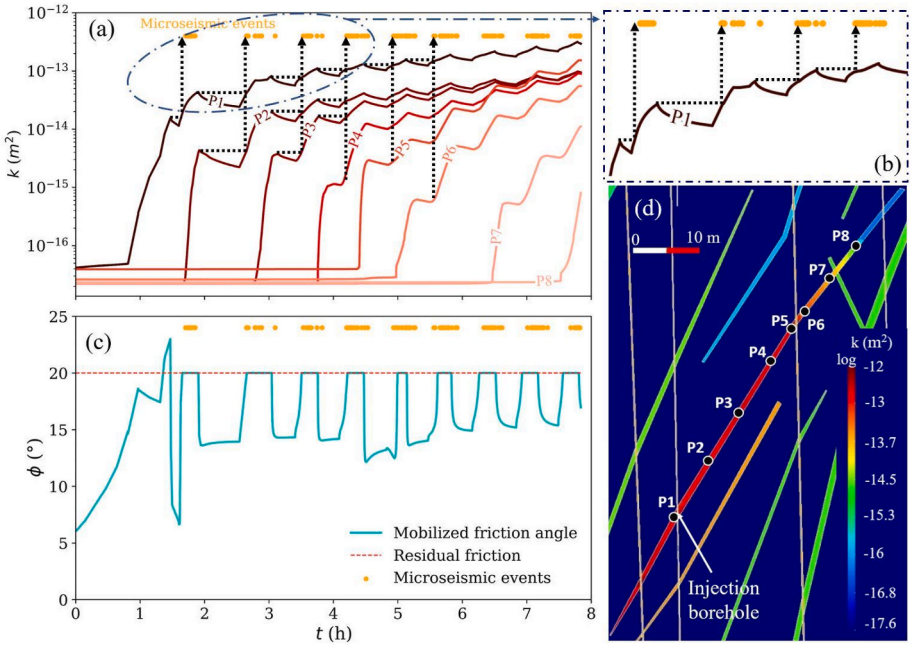

Fig. 10. a) Temporal evolution of permeability at 8 points (indicated in (d)) along the fracture together with timestamps of the microseismic events. The sharp permeability increase indicates when the pressure perturbation front reaches each point. b) Zoomed view of permeability evolution at point 1 to highlight the relation between permeability enhancement and microseismic threshold. c) Mobilized friction angle (Eq. (10)) during injection at point P1. d) Location of the 8 control points along the fracture, with the permeability contour plot after 8 h of stimulation in the background. As a reference, point P8 is located 50 m away from the injection well.

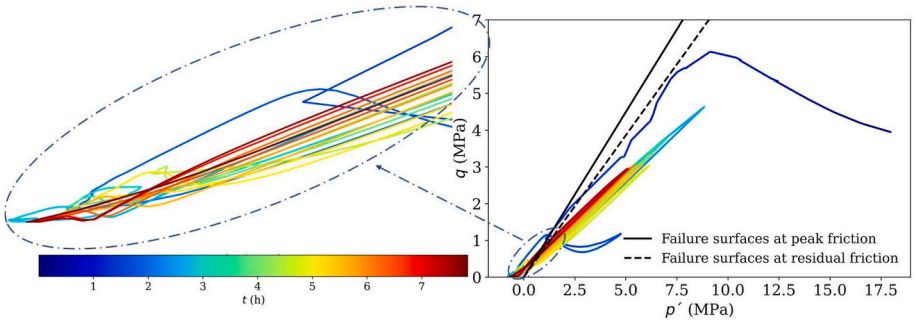

Fig. 11. Stress path at point 1 as in Fig. 7 for the larger number of injection cycles with a zoom in the critical area. The failure surfaces at peak and residual friction are based on Mohr-Coulomb failure criterion.

injection-induced fracture aperture changes (Embedded models; EE and VE), pore pressure diffusion occurs slowly away from the stimulated fracture patch because of the low initial fracture permeability. Fracture opens up where pore pressure increases, and an additional dilation occurs in model VE when shear failure conditions are reached, yielding a progressively fracture stimulation in which permeability is enhanced.[14,72,73] The effect of the additional permeability enhancement caused by slip is evident when comparing the pore pressure profiles of models EE and VE, i.e., pressure build-up is lower in the viscoplastic model than in the elastic one.

Reducing the effective normal stress causes shear displacement, dilation and permeability enhancement of the natural fracture. Almost 90% of the slip displacement and dilation is estimated to occur after fracture shear failure.[74] After fracture activation, stress trajectories in the stimulated fracture follow a similar pattern in each injection cycle, i.e. decreasing both effective normal and deviatoric stress during injection and increasing again to a similar state developing fracture reactivation (Fig. 7). This pattern would be observed in points far away from the injection borehole after enough time for the reactivation front to reach distant points. These reactivation cycles are matched with the timestamps of seismic events.

When stimulating a fracture, the perturbation is not restricted to the fracture itself because (1) pore pressure diffuses, mainly through fractures, (2) induced poromechanical strain-stress changes extend further away than the stimulated fracture, and (3) shear stress transfer modifies the state of stress around the slipped patch of the fracture (Fig. 8c), which may either promote shear failure of nearby fractures or inhibit it (stress shadow).[23] When shear slip occurs along a fracture, the stress drop is right-lateral (blue colors in Fig. 8c). The induced right-lateral shear stress is not restricted to the slipped patch and forms two lobes at the tips of the slipped area that affect portions of nearby fractures, creating the so-called stress shadow,[75] which inhibits shear slip of these regions. The phenomenon of stress shadow refers to the development of a localized area exhibiting high compressive stresses that are oriented perpendicular to the fracture face in the vicinity of the fracture center. This results in the reorientation of the direction of maximum stress within the region of the stress shadow.[76] Thus, if subsequent hydraulic stimulations are performed in nearby fractures, the portions affected by the stress shadow may not be reactivated and permeability enhancement would be limited. On the contrary, the areas affected by the yellow-reddish colors in Fig. 8c experience left-lateral shear stress that favors subsequent fracture reactivation if these fractures are stimulated. Note that the fractures placed close to the stimulated fracture contain both areas where shear slip is either promoted or inhibited.

The primary mechanism behind the manifestation of microseismic events is explicable by means of hydroshearing of pre-existing natural fractures that reach failure conditions.[77] Induced microseismicity is a phenomenon naturally accompanying plastic, i. e, irreversible, deformations. The involved hydromechanical processes including pressure increase, fracture dilation, permeability enhancement, and consequent microseismicity are well captured by our fully coupled viscoplastic model. The similar timestamps of plastic dilation (and pertinent permeability enhancement) and microseismic events (Fig. 10) further support the model. Minakov and Yarushina[78] have developed a poro-elastoplastic model to clarify the connection between the components of the seismic moment tensor and the failure process through the analysis of the acoustic emission during rock deformation. The model connects the localized failure pattern, plastic dilation ($\sin\psi$), and corresponding seismic response. Plasticity can explain induced microseismic source mechanisms. Further studies should focus on finding correlations between the spatiotemporal development of microseismicity (subject to the accuracy of the monitoring network) and the extent of the zone suffering from viscoplastic instability.

In induced seismicity, a hysteresis phenomenon known as the Kaiser effect,[70] is frequently observed.[79,80] This effect is characterized by the gradual failure of a material subjected to a series of increasing amplitude loading cycles, wherein subsequent failures typically occur at stress levels exceeding those reached in prior cycles. This effect elucidates the observation that acoustic emissions during rock failure cease when stress levels decrease and only resume once the medium is reloaded to its previous maximum.[78] It is anticipated that the Kaiser effect exhibits significant impact within a singular injection stage but displays lesser relevance between successive stages (multi-stage injection).

Modeling hydraulic stimulation presents challenges due to the involvement of complex physical processes, such as rock deformation, fluid flow, and fracture initiation and propagation.[81,82] The complexity of hydraulic stimulation arises from several factors, such as the coupling of fluid flow inside fractures with rock and fracture deformation; the involvement of multiscale and multi-physics processes like the interaction between natural and hydraulic fractures, leak-off, and rock heterogeneity; and the difficulty in accurately modeling geological and operational conditions due to limited data availability and high costs. The challenge remains in scaling up numerical simulation capabilities from single fracture stimulation in a laboratory setting to multiple fractures at the field scale in industrial projects. This upscaling necessitates the development of more efficient numerical methods that can effectively manage the increased demand for computational resources. In order to make the study of hydraulic stimulation more tractable, some aspects of the problem need to be simplified or ignored in numerical simulations, leading to the development of multiple modeling approaches with varying applicability and limitations. Though a 3D model is more attributable to a specific geological condition (such a case in this study), it involves huge computational cost. A 2D model gives useful insights and information elaborating our understanding of the involved processes and helping us to improve hydraulic stimulation designs. We show that a viscoplastic model that accounts for strength weakening, dilatancy, and fracture permeability evolution as a function of volumetric strain enables numerical models to accurately reproduce hydraulic stimulation in crystalline rocks, thereby enhancing the understanding of the underlying processes and improving the capability to forecast hydraulic stimulation outcomes.

5. Conclusions

We have modeled one of the hydraulic stimulations performed at the BULGG using three different approaches. Despite reproducing a well-fitted pressure evolution curve, the model with manually calibrated permeability lacks the ability to capture the pore pressure distribution along the fracture, and consequently the poromechanical response at the rock matrix and nearby fractures, because permeability is assumed homogeneous along the fracture. Considering the embedded model to simulate permeability enhancement following the cubic law as a function of the volumetric strain improves the estimation of the spatiotemporal distribution of pressure. Yet, pressure is overestimated after the onset of fracture slips when assuming elastic behavior. To satisfactorily reproduce field measurements, an additional permeability enhancement is required in the post-failure stage, which is achieved with a viscoplastic model with strain weakening and dilatancy. This viscoplastic model, whose parameters have been manually adjusted to render a good fit of the early stages of stimulation, has been validated by extending the simulation to further injection cycles. Microseismic events in each cycle occur once plastic strain and, thus, permeability surpass the maximum value achieved in previous injection cycles. Furthermore, post-injection microseismicity becomes more perceptible as injection cycles accumulate. The timestamps of monitored microseismic events are well predicted by the viscoplastic model, which predicts unstable conditions at the time of the seismic clouds showing that the induced microseismic threshold is concomitant to plasticity. The correlation between plasticity and induced microseismic events is illustrated by stress trajectories, which show that the timestamps of monitored microseismicity at the field laboratory coincide with the periods at which the fracture undergoes shear failure conditions. Furthermore, the

viscoplastic model reproduces the coupled processes in a natural way, thus avoiding the tedious, subjective and prone-to-error manual calibration of the spatio-temporal evolution of permeability.

In summary, the proposed VE model accounts for fracture reactivation and dilatancy and allows good reproduction of observed pressure evolution, three orders of magnitude irreversible increases in permeability and the timing of microseismic events. We conclude that the insights yielded by this model are supported by observations. We conjecture that they can be extended beyond the processes and extent of the hydraulic stimulation, into a comprehensive understanding of the hydromechanical response of the subsurface to fluid injection and associated (micro) seismicity.

Open research

The extensively validated fully-coupled finite element numerical code, CODE_BRIGHT, can be accessed at the developer page: https://deca.upc.edu/en/projects/code_bright together with the user's guide and numerous tutorials.

Data can be accessed at: https://digital.csic.es/handle/10261/311769.

CRediT authorship contribution statement

Iman Vaezi: Data curation, Formal analysis, Investigation, Methodology, Software, Validation, Visualization, Writing – original draft, Writing – review & editing. **Andrés Alcolea:** Conceptualization, Data curation, Formal analysis, Investigation, Resources, Software, Writing – review & editing. **Peter Meier:** Data curation, Funding acquisition, Resources. **Francesco Parisio:** Formal analysis, Writing – review & editing. **Jesus Carrera:** Formal analysis, Writing – review & editing. **Víctor Vilarrasa:** Conceptualization, Formal analysis, Funding acquisition, Investigation, Methodology, Project administration, Software, Supervision, Writing – review & editing.

Declaration of competing interest

The authors declare that they have no known competing financial interests or personal relationships that could have appeared to influence the work reported in this paper.

Data availability

Data can be accessed at: https://digital.csic.es/handle/10261/311769

Acknowledgements and data

I.V. and V.V. acknowledge funding from the European Research Council (ERC) under the European Union's Horizon 2020 Research and Innovation Program through the Starting Grant GEoREST (www.georest.eu), under grant agreement No. 801809. The work of Geo-Energie Suisse AG was financially supported by the Swiss Federal Office of Energy within the framework of the ZoDrEx GEOTHERMICA project under contract SI/501720-01. F.P. and V.V. acknowledge funding from the European Union's Horizon 2020 Research and Innovation Program through the Marie Sklowdowska-Curie Individual Fellowship ARMISTICE, under Grant Agreement No. 882733. J.C. and V.V. acknowledges financial support from the "ZoDrEx" project, which has been subsidized through the ERANET Cofund GEOTHERMICA (Project No. 731117), from the European Commission and the Spanish Ministry of Economy, Industry and Competitiveness (MINECO). IMEDEA is an accredited "Maria de Maeztu Excellence Unit" (Grant CEX2021-001198, funded by MCIN/AEI/10.13039/501100011033). IDAEA-CSIC is a Center of Excellence Severo Ochoa (Spanish Ministry of Science and Innovation, Project CEX2018-000794-S).

Appendix A. Supplementary data

Supplementary data to this article can be found online at https://doi.org/10.1016/j.ijrmms.2024.105689.

References

1. Pruess K. Enhanced geothermal systems (EGS) using CO2 as working fluid—a novel approach for generating renewable energy with simultaneous sequestration of carbon. *Geothermics*. 2006;35(4):351–367. https://doi.org/10.1016/j.geothermics.2006.08.002.
2. Randolph JB, Saar MO. Combining geothermal energy capture with geologic carbon dioxide sequestration. *Geophys Res Lett*. 2011;38(10). https://doi.org/10.1029/2011GL047265.
3. Brown DW, Duchane DV, Heiken G, Hriscu VT. *Mining the Earth's Heat: Hot Dry Rock Geothermal Energy*. Springer Science & Business Media; 2012.
4. Olasolo P, Juárez MC, Morales MP, D'Amico S, Liarte IA. Enhanced geothermal systems (EGS): a review. *Renew Sustain Energy Rev*. 2016;56:133–144. https://doi.org/10.1016/j.rser.2015.11.031.
5. Baria R, Baumgärtner J, Rummel F, Pine RJ, Sato Y. HDR/HWR reservoirs: concepts, understanding and creation. *Geothermics*. 1999;28(4):533–552. https://doi.org/10.1016/S0375-6505(99)00045-0.
6. Breede K, Dzebisashvili K, Liu X, Falcone G. A systematic review of enhanced (or engineered) geothermal systems: past, present and future. *Geotherm Energy*. 2013;1(1):4. https://doi.org/10.1186/2195-9706-1-4.
7. Gan Q, Elsworth D. Analysis of fluid injection-induced fault reactivation and seismic slip in geothermal reservoirs. *J Geophys Res Solid Earth*. 2014;119(4):3340–3353. https://doi.org/10.1002/2013JB010679.
8. Pine RJ, Batchelor AS. Downward migration of shearing in jointed rock during hydraulic injections. *Int J Rock Mech Min Sci Geomech Abstracts*. 1984;21(5):249–263. https://doi.org/10.1016/0148-9062(84)92681-0.
9. Townend J, Zoback MD. How faulting keeps the crust strong. *Geology*. 2000;28(5):399–402.
10. Achtziger-Zupančič P, Loew S, Mariéthoz G. A new global database to improve predictions of permeability distribution in crystalline rocks at site scale. *J Geophys Res Solid Earth*. 2017;122(5):3513–3539. https://doi.org/10.1002/2017JB014106.
11. Ingebritsen SE, Manning CE. Permeability of the continental crust: dynamic variations inferred from seismicity and metamorphism. *Geofluids*. 2010;10(1-2):193–205. https://doi.org/10.1111/j.1468-8123.2010.00278.x.
12. Manga M, Beresnev I, Brodsky EE, et al. Changes in permeability caused by transient stresses: field observations, experiments, and mechanisms. *Rev Geophys*. 2012;50(2). https://doi.org/10.1029/2011RG000382.
13. Riahi A, Damjanac B. Numerical study of hydro-shearing in geothermal reservoirs with a pre-existing discrete fracture network. In: *Proceedings of the 38th Workshop on Geothermal Reservoir Engineering*. 2013:11–13. Stanford, CA.
14. Ye Z, Ghassemi A. Injection-induced shear slip and permeability enhancement in granite fractures. *J Geophys Res Solid Earth*. 2018;123(10):9009–9032. https://doi.org/10.1029/2018JB016045.
15. Rutqvist J, Birkholzer J, Cappa F, Tsang CF. Estimating maximum sustainable injection pressure during geological sequestration of CO2 using coupled fluid flow and geomechanical fault-slip analysis. *Energy Convers Manag*. 2007;48(6):1798–1807. https://doi.org/10.1016/j.enconman.2007.01.021.
16. Safari R, Ghassemi A. 3D thermo-poroelastic analysis of fracture network deformation and induced micro-seismicity in enhanced geothermal systems. *Geothermics*. 2015;58:1–14. https://doi.org/10.1016/j.geothermics.2015.06.010.
17. Vilarrasa V, De Simone S, Carrera J, Villaseñor A. Unraveling the causes of the seismicity induced by underground gas storage at Castor, Spain. *Geophys Res Lett*. 2021;48(7), e2020GL092038. https://doi.org/10.1029/2020GL092038.
18. Ellsworth WL. Injection-induced earthquakes. *Science*. 2013;341(6142), 1225942. https://doi.org/10.1126/science.1225942.
19. Evans KF, Genter A, Sausse J. Permeability creation and damage due to massive fluid injections into granite at 3.5 km at Soultz: 1. Borehole observations. *J Geophys Res Solid Earth*. 2005;110(B4). https://doi.org/10.1029/2004JB003168.
20. Guglielmi Y, Cappa F, Avouac JP, Henry P, Elsworth D. Seismicity triggered by fluid injection–induced aseismic slip. *Science*. 2015;348(6240):1224–1226. https://doi.org/10.1126/science.aab0476.
21. Kim WY. Induced seismicity associated with fluid injection into a deep well in Youngstown, Ohio. *J Geophys Res Solid Earth*. 2013;118(7):3506–3518. https://doi.org/10.1002/jgrb.50247.
22. Majer EL, Baria R, Stark M, et al. Induced seismicity associated with enhanced geothermal systems. *Geothermics*. 2007;36(3):185–222. https://doi.org/10.1016/j.geothermics.2007.03.003.
23. Safari R, Ghassemi A. Three-dimensional poroelastic modeling of injection induced permeability enhancement and microseismicity. *Int J Rock Mech Min Sci*. 2016;84:47–58. https://doi.org/10.1016/j.ijrmms.2015.12.007.
24. Vilarrasa V, Carrera J, Olivella S, Rutqvist J, Laloui L. Induced seismicity in geologic carbon storage. *Solid Earth*. 2019;10(3):871–892. https://doi.org/10.5194/se-10-871-2019.
25. Vilarrasa V, Koyama T, Neretnieks I, Jing L. Shear-induced flow channels in a single rock fracture and their effect on solute transport. *Transport Porous Media*. 2011;87(2):503–523. https://doi.org/10.1007/s11242-010-9698-1.
26. Mallikamas W, Rajaram H. On the anisotropy of the aperture correlation and effective transmissivity in fractures generated by sliding between identical self-

affine surfaces. *Geophys Res Lett*. 2005;32(11). https://doi.org/10.1029/2005GL022859.
27. Kc B, Ghazanfari E. Geothermal reservoir stimulation through hydro-shearing: an experimental study under conditions close to enhanced geothermal systems. *Geothermics*. 2021;96, 102200. https://doi.org/10.1016/j.geothermics.2021.102200.
28. Meng M, Frash LP, Li W, et al. Hydro-mechanical measurements of sheared crystalline rock fractures with applications for EGS collab experiments 1 and 2. *J Geophys Res Solid Earth*. 2022;127(2), e2021JB023000. https://doi.org/10.1029/2021JB023000.
29. Rinaldi AP, Rutqvist J, Sonnenthal EL, Cladouhos TT. Coupled THM modeling of hydroshearing stimulation in tight fractured volcanic rock. *Transport Porous Media*. 2015;108(1):131–150. https://doi.org/10.1007/s11242-014-0296-5.
30. Bunger AP, McLennan J, Jeffrey R. *Effective and Sustainable Hydraulic Fracturing*. InTech; 2013.
31. Rahman MK, Hossain MM, Rahman SS. A shear-dilation-based model for evaluation of hydraulically stimulated naturally fractured reservoirs. *Int J Numer Anal Methods GeoMech*. 2002;26(5):469–497. https://doi.org/10.1002/nag.208.
32. Willis-Richards J, Watanabe K, Takahashi H. Progress toward a stochastic rock mechanics model of engineered geothermal systems. *J Geophys Res Solid Earth*. 1996;101(B8):17481–17496. https://doi.org/10.1029/96JB00882.
33. Grigoli F, Cesca S, Priolo E, et al. Current challenges in monitoring, discrimination, and management of induced seismicity related to underground industrial activities: a European perspective. *Rev Geophys*. 2017;55(2):310–340. https://doi.org/10.1002/2016RG000542.
34. Kraft T, Mai PM, Wiemer S, et al. Enhanced geothermal systems: mitigating risk in urban areas. *Eos, Transactions American Geophysical Union*. 2009;90(32):273–274. https://doi.org/10.1029/2009EO320001.
35. Kumari WGP, Ranjith PG. Sustainable development of enhanced geothermal systems based on geotechnical research – a review. *Earth Sci Rev*. 2019;199, 102955. https://doi.org/10.1016/j.earscirev.2019.102955.
36. Guglielmi Y, Elsworth D, Cappa F, et al. In situ observations on the coupling between hydraulic diffusivity and displacements during fault reactivation in shales. *J Geophys Res Solid Earth*. 2015;120(11):7729–7748. https://doi.org/10.1002/2015JB012158.
37. Amann F, Gischig V, Evans K, et al. The seismo-hydromechanical behavior during deep geothermal reservoir stimulations: open questions tackled in a decameter-scale in situ stimulation experiment. *Solid Earth*. 2018;9(1):115–137. https://doi.org/10.5194/se-9-115-2018.
38. David C, Wassermann J, Amann F, et al. KG^{2}B, a collaborative benchmarking exercise for estimating the permeability of the Grimsel granodiorite – Part 1: measurements, pressure dependence and pore-fluid effects. *Geophys J Int*. 2018;215(2):799–824. https://doi.org/10.1093/gji/ggy304.
39. David C, Wassermann J, Amann F, et al. KG^{2}B, a collaborative benchmarking exercise for estimating the permeability of the Grimsel granodiorite—Part 2: modelling, microstructures and complementary data. *Geophys J Int*. 2018;215(2):825–843. https://doi.org/10.1093/gji/ggy305.
40. Meier P, Guinot F, Bethmann F, et al. ZoDrEx an European endeavour for optimising zonal isolation, drilling and exploitation of EGS projects. In: *Proceedings World Geothermal Congress*. 2020:1.
41. Meier PM, Serbeto F, Christe F, et al. Results from benchmark testing of zonal isolation borehole completions for multi-stage EGS stimulation in the bedretto underground rock laboratory in Switzerland. *OnePetro*. 2022. https://doi.org/10.56952/ARMA-2022-0292.
42. Bröker K, Ma X. Estimating the least principal stress in a granitic rock mass: systematic mini-frac tests and elaborated pressure transient analysis. *Rock Mech Rock Eng*. 2022;55(4):1931–1954. https://doi.org/10.1007/s00603-021-02743-1.
43. David C, Nejati M, Geremia D. *On Petrophysical and Geomechanical Properties of Bedretto Granite*. ETH Zurich; 2020.
44. Gischig VS, Giardini D, Amann F, et al. Hydraulic stimulation and fluid circulation experiments in underground laboratories: stepping up the scale towards engineered geothermal systems. *Geomechanics for Energy and the Environment*. 2020;24, 100175. https://doi.org/10.1016/j.gete.2019.100175.
45. Ma X, Hertrich M, Amann F, et al. Multi-disciplinary characterizations of the BedrettoLab – a new underground geoscience research facility. *Solid Earth*. 2022;13(2):301–322. https://doi.org/10.5194/se-13-301-2022.
46. Ma X, Doonechaly NG, Hertrich M, Gischig V, Klee G. Preliminary in situ stress and fracture characterization in the bedretto underground laboratory, Swiss Alps: implications on hydraulic stimulation. In: *Rock Mechanics for Natural Resources and Infrastructure Development*. CRC Press; 2019:1559–1567.
47. Shakas A, Maurer H, Giertzuch PL, et al. Permeability enhancement from a hydraulic stimulation imaged with ground penetrating radar. *Geophys Res Lett*. 2020;47(17), e2020GL088783. https://doi.org/10.1029/2020GL088783.
48. Taron J, Elsworth D. Thermal–hydrologic–mechanical–chemical processes in the evolution of engineered geothermal reservoirs. *Int J Rock Mech Min Sci*. 2009;46(5):855–864. https://doi.org/10.1016/j.ijrmms.2009.01.007.
49. Olivella S, Gens A, Carrera J, Alonso EE. Numerical formulation for a simulator (CODE_BRIGHT) for the coupled analysis of saline media. *Eng Comput*. 1996;13(7):87–112. https://doi.org/10.1108/02644409610151575.
50. Olivella S, Carrera J, Gens A, Alonso EE. Nonisothermal multiphase flow of brine and gas through saline media. *Transport Porous Media*. 1994;15(3):271–293. https://doi.org/10.1007/BF00613282.
51. Zimmerman RW. Coupling in poroelasticity and thermoelasticity. *Int J Rock Mech Min Sci*. 2000;37(1):79–87. https://doi.org/10.1016/S1365-1609(99)00094-5.
52. Zienkiewicz OC, Taylor RL. *The Finite Element Method: Solid Mechanics*. vol. 2. Butterworth-heinemann; 2000.
53. Zienkiewicz OC, Cormeau IC. Visco-plasticity—plasticity and creep in elastic solids—a unified numerical solution approach. *Int J Numer Methods Eng*. 1974;8(4):821–845.
54. Vilarrasa V, Bolster D, Olivella S, Carrera J. Coupled hydromechanical modeling of CO2 sequestration in deep saline aquifers. *Int J Greenh Gas Control*. 2010;4(6):910–919. https://doi.org/10.1016/j.ijggc.2010.06.006.
55. Hughes TJR, Taylor RL. Unconditionally stable algorithms for quasi-static elasto/visco-plastic finite element analysis. *Comput Struct*. 1978;8(2):169–173. https://doi.org/10.1016/0045-7949(78)90019-6.
56. Witherspoon PA, Wang JSY, Iwai K, Gale JE. Validity of Cubic Law for fluid flow in a deformable rock fracture. *Water Resour Res*. 1980;16(6):1016–1024. https://doi.org/10.1029/WR016i006p01016.
57. Häring MO, Schanz U, Ladner F, Dyer BC. Characterisation of the Basel 1 enhanced geothermal system. *Geothermics*. 2008;37(5):469–495. https://doi.org/10.1016/j.geothermics.2008.06.002.
58. Ladner F, Häring MO. Hydraulic characteristics of the basel 1 enhanced geothermal system. *GRC Transactions*. 2009;33:199–203.
59. De Simone S, Carrera J. Analytical solutions to coupled HM problems to highlight the nonlocal nature of aquifer storage. *Water Resour Res*. 2017;53(11):9580–9599. https://doi.org/10.1002/2017WR020824.
60. Ramos G, Carrera J, Gómez S, Minutti C, Camacho R. A stable computation of log-derivatives from noisy drawdown data. *Water Resour Res*. 2017;53(9):7904–7916. https://doi.org/10.1002/2017WR020811.
61. Bourdet D, Whittle TM, Douglas AA, Pirard YM. A new set of type curves simplifies well test analysis. *World Oil*. 1983;196(6):95–106.
62. Vilarrasa V, De Simone S, Carrera J, Villaseñor A. Multiple induced seismicity mechanisms at Castor underground gas storage illustrate the need for thorough monitoring. *Nat Commun*. 2022;13(1):3447. https://doi.org/10.1038/s41467-022-30903-6.
63. Xie L, Min KB. Initiation and propagation of fracture shearing during hydraulic stimulation in enhanced geothermal system. *Geothermics*. 2016;59:107–120. https://doi.org/10.1016/j.geothermics.2015.10.012.
64. Goertz-Allmann BP, Goertz A, Wiemer S. Stress drop variations of induced earthquakes at the Basel geothermal site. *Geophys Res Lett*. 2011;38(9). https://doi.org/10.1029/2011GL047498.
65. Kim KI, Yoo H, Park S, et al. Induced and triggered seismicity by immediate stress transfer and delayed fluid migration in a fractured geothermal reservoir at Pohang, South Korea. *Int J Rock Mech Min Sci*. 2022;153, 105098. https://doi.org/10.1016/j.ijrmms.2022.105098.
66. Yoo H, Park S, Xie L, et al. Hydro-mechanical modeling of the first and second hydraulic stimulations in a fractured geothermal reservoir in Pohang, South Korea. *Geothermics*. 2021;89, 101982. https://doi.org/10.1016/j.geothermics.2020.101982.
67. De Simone S, Vilarrasa V, Carrera J, Alcolea A, Meier P. Thermal coupling may control mechanical stability of geothermal reservoirs during cold water injection. *Phys Chem Earth, Parts A/B/C*. 2013;64:117–126. https://doi.org/10.1016/j.pce.2013.01.001.
68. Baisch S, Vörös R. Reservoir induced seismicity: where, when, why and how strong. In: *Proceedings World Geothermal Congress*. 2010.
69. Wang X, Liu D, Li X, Gao Q. Mechanism and implications of shut-in induced earthquakes. *Alex Eng J*. 2023;65:837–846. https://doi.org/10.1016/j.aej.2022.09.042.
70. Lavrov A. The Kaiser effect in rocks: principles and stress estimation techniques. *Int J Rock Mech Min Sci*. 2003;40(2):151–171. https://doi.org/10.1016/S1365-1609(02)00138-7.
71. Kim T, Avouac JP. Stress-based and convolutional forecasting of injection-induced seismicity: application to the otaniemi geothermal reservoir stimulation. *J Geophys Res Solid Earth*. 2023;128(4), e2022JB024960. https://doi.org/10.1029/2022JB024960.
72. Simpson G, Guéguen Y, Schneider F. Permeability enhancement due to microcrack dilatancy in the damage regime. *J Geophys Res Solid Earth*. 2001;106(B3):3999–4016. https://doi.org/10.1029/2000JB900194.
73. Peach CJ, Spiers CJ. Influence of crystal plastic deformation on dilatancy and permeability development in synthetic salt rock. *Tectonophysics*. 1996;256(1):101–128. https://doi.org/10.1016/0040-1951(95)00170-0.
74. Xiao Y, Guo J, Wang H, Lu L, Chen M. Elastoplastic constitutive model for hydraulic aperture analysis of hydro-shearing in geothermal energy development. *Simulation*. 2019;95(9):861–872. https://doi.org/10.1177/0037549718793216.
75. Taghichian A, Zaman M, Devegowda D. Stress shadow size and aperture of hydraulic fractures in unconventional shales. *J Petrol Sci Eng*. 2014;124:209–221. https://doi.org/10.1016/j.petrol.2014.09.034.
76. Waters G, Dean B, Downie R, Kerrihard K, Austbo L, McPherson B. Simultaneous hydraulic fracturing of adjacent horizontal wells in the woodford shale. *OnePetro*. 2009. https://doi.org/10.2118/119635-MS.
77. Yoon JS, Zang A, Stephansson O, Hofmann H, Zimmermann G. Discrete element modelling of hydraulic fracture propagation and dynamic interaction with natural fractures in hard rock. *Procedia Eng*. 2017;191:1023–1031. https://doi.org/10.1016/j.proeng.2017.05.275.
78. Minakov A, Yarushina V. Elastoplastic source model for microseismicity and acoustic emission. *Geophys J Int*. 2021;227(1):33–53. https://doi.org/10.1093/gji/ggab207.
79. Baisch S, Vörös R, Rothert E, Stang H, Jung R, Schellschmidt R. A numerical model for fluid injection induced seismicity at Soultz-sous-Forêts. *Int J Rock Mech Min Sci*. 2010;47(3):405–413. https://doi.org/10.1016/j.ijrmms.2009.10.001.

80. Dempsey D, Riffault J. Response of induced seismicity to injection rate reduction: models of delay, decay, quiescence, recovery, and Oklahoma. *Water Resour Res*. 2019;55(1):656–681. https://doi.org/10.1029/2018WR023587.
81. Chen B, Barboza BR, Sun Y, et al. A review of hydraulic fracturing simulation. *Arch Comput Methods Eng*. 2022;29(4):1–58. https://doi.org/10.1007/s11831-021-09653-z.
82. Wu Z, Cui C, Jia P, Wang Z, Sui Y. Advances and challenges in hydraulic fracturing of tight reservoirs: a critical review. *Energy Geoscience*. 2022;3(4):427–435. https://doi.org/10.1016/j.engeos.2021.08.002.